Novel Approach for Experimental Measurement of Sectional Stiffness Properties of Composite Rotor Blades

Tyler Sinotte
tsinotte@umd.edu
Graduate Research Assistant

Olivier A. Bauchau
obauchau@umd.edu
Sikorsky Professor of Rotorcraft

Alfred Gessow Rotorcraft Center
University of Maryland
College Park, MD, USA

ABSTRACT

A novel experimental-numerical technique is presented for evaluating the full 6 × 6 stiffness matrices for beams. The general formulation makes the method well suited for isotropic beams with simple cross-sectional configurations or beams made of anisotropic materials with complex geometries, as typically exhibited in composite rotor blades. A 2-D finite element code, *SectionBuilder*, is used to generate a finite element mesh of the cross-section and evaluate the warping field. The surface strain field is experimentally measured along the span of the beams using Digital Image Correlation (DIC). Stiffness matrices are then calculated based on the experimentally measured strain data and numerical model of the cross-section, with results presented for an isotropic beam, a composite beam with bending/torsion coupling, and a composite rotor blade.

1. NOTATION

$\underline{\underline{A}}_L$, $\underline{\underline{B}}_L$	Strain interpolation matrices
$\underline{\mathcal{F}}$	Stress resultant vector
$\underline{\underline{K}}$	6 × 6 cross-sectional stiffness matrix
L	Number of load cases
N	Number of strain measurements
$\underline{\underline{S}}$	6 × 6 cross-sectional compliance matrix
$\underline{\underline{W}}$	Cross-sectional warping matrix
$\underline{\underline{Z}}$	Cross-sectional coordinate matrix
l	Beam length
t	Beam thickness
w	Beam width
α_2,α_3	Cross-sectional coordinates in chordwise and flapwise directions
$\underline{\epsilon}$	Strain vector
$\tilde{\mathcal{K}}$	Curvature tensor

2. INTRODUCTION

Typically, the dynamic response of a rotorcraft is predicted from a comprehensive analysis, such as RCAS or Dymore, that uses beam formulations to represent the rotor blades. Over the past several decades, significant improvements have been made in comprehensive analysis capabilities, such as higher fidelity aerodynamic models, CFD/CSD coupling, geometrically exact beam formulations, and flexible multibody dynamic formulations. In addition, experimental efforts, such as the UH-60A Airloads program,[1] have provided useful databases from which to validate many of these analysis capabilities.

However, uncertainties still exist in the sectional stiffness properties of composite blades, which can strongly affect blade dynamics, structural couplings, and predicted stress and strain fields. Although multiple computational tools currently exist for evaluating the sectional properties of composite blades based on geometry, the actual blade will vary from the designed blade due to variabilities in the manufacturing process and material properties. Therefore, a means of predicting the sectional stiffness properties from the actual manufactured blades is needed to better predict the detailed stress and strain fields within the blade.

While several experimental techniques exist for predicting sectional properties, most rely on measuring the beam displacements or rotations and using simplified beam models to calculate the average stiffness of the entire blade. These methods have been applied to rotor blades, with examples including measurements of the Hart I[2] and Hart II[3] blades, and measurements of individual components of a notional wind turbine.[4] While these methods have proven effective for measuring the bending and torsional stiffness, large discrepancies can arise due to non-uniform blades or if the experimental boundary conditions are modeled poorly. Moreover, these methods require separate equations to be derived to account for the complex structural couplings that can be present in composite blades.

In this work, a different approach is used, in which the strain field over the surface of a blade is measured for a

---

Presented at the 45th European Rotorcraft Forum, Warsaw, Poland, September 17–20, 2019.

known static loading, which is possible with non-contact optical strain measurement techniques. Several of these non-contact measurement techniques have already been applied to rotorcraft systems, including Projection Moire Interferometry[5, 6] and Digital Image Correlation (DIC),[7] with DIC used for the current study. Since the strain measurements can be obtained on the entire surface of the span, span-wise variations in properties can be predicted, as opposed to just an effective, or average, stiffness of the entire structure. In addition, because the strain field is controlled primarily by the forces and moments applied to the beam, the boundary conditions should only impact the measurements in the form of edge effects in the measured strain fields.

The goal of this paper is therefore to present a novel numerical-experimental technique for prediction of the complete stiffness matrix of composite rotor blades. Preliminary experimental results are presented for beams made of both isotropic and composite materials. While the emphasis of the paper focuses on the stiffness matrix calculations, the experimental strain database generated during testing can also be used for future validation of the post-processing tools for comprehensive analyses, such as *SectionBuilder* and *VABS*, as well as for 3-D finite element tools, such as *X3D*.

3. STIFFNESS MATRIX CALCULATION

This section summarizes a general procedure for calculating the stiffness matrix, based on an experimental measurement of the strain field at the surface of a specimen under a known loading.

3.1. Theoretical background

The analysis approach relies on the solution strategy for beams featuring complex cross-sections with anisotropic composite materials first presented by Giavotto *et al.*[8] Based on Hamilton's canonical formulation, the exact solution can be decomposed into a central and extremity solution which forms the foundation for *SectionBuilder*.[9, 10] The extremity solutions become negligible far from the beam's edges and the central solution is therefore an exact solution of the linear theory of 3-D elasticity away from the edges. An important feature of the central solution is that the 3-D strain tensor at any point in the cross-section, denoted by $\underline{\epsilon}$, is proportional to the stress resultants, denoted by $\underline{\mathcal{F}}$, according to

$$\underline{\epsilon} = \left[\underline{\underline{A}}_L (\underline{\underline{Z}}\,\underline{\underline{S}} + \underline{\underline{W}}\tilde{\mathcal{K}}^T) + \underline{\underline{B}}_L \underline{\underline{W}} \right] \underline{\mathcal{F}}. \tag{1}$$

where $\underline{\underline{A}}_L$ and $\underline{\underline{B}}_L$ are the strain interpolation matrices, $\underline{\underline{Z}}$ is a matrix representation of the cross-sectional coordinates α_2 and α_3, $\underline{\underline{S}}$ is the 6 x 6 sectional compliance matrix, $\underline{\underline{W}}$ is the warping field of the cross-section under unit loads in each direction, and $\tilde{\mathcal{K}}$ is the curvature tensor. The strain tensor is partitioned into out-of-plane and in-plane components by $\underline{\epsilon}^T = \{\epsilon_{11}, \epsilon_{12}, \epsilon_{13}, \epsilon_{22}, \epsilon_{33}, \epsilon_{23}\}$ and the stress resultants are partitioned according to $\underline{\mathcal{F}}^T = \left\{\underline{F}^T, \underline{M}^T\right\}$, where $\underline{F}$ consists of the axial force and two transverse shear forces and $\underline{M}$ consists of the twisting moment and two bending moments.

3.2. Governing equations

In order to calculate the sectional stiffness matrix, Eq. 1 must first be solved for the sectional compliance matrix $\underline{\underline{S}}$. For a discrete location within the cross-section, denoted by $(\cdot)_i$, the strain under a given loading, denoted by $(\cdot)^{(j)}$, can be expressed from Eq. (1) as

$$\underline{\epsilon}_i^{(j)} = \underline{\underline{U}}_i \underline{\underline{S}}\,\underline{\mathcal{F}}^{(j)} + \underline{\underline{V}}_i \underline{\mathcal{F}}^{(j)} \tag{2}$$

where $\underline{\underline{U}}_i$ and $\underline{\underline{V}}_i$ are 6×6 matrices defined by

$$\underline{\underline{U}}_i = \underline{\underline{A}}_{L,i} \underline{\underline{Z}}_i = \begin{bmatrix} 1 & 0 & 0 & 0 & \alpha_3 & -\alpha_2 \\ 0 & 1 & 0 & -\alpha_3 & 0 & 0 \\ 0 & 0 & 1 & \alpha_2 & 0 & 0 \\ 0 & 0 & 0 & 0 & 0 & 0 \\ 0 & 0 & 0 & 0 & 0 & 0 \\ 0 & 0 & 0 & 0 & 0 & 0 \end{bmatrix} \tag{3a}$$

$$\underline{\underline{V}}_i = \underline{\underline{A}}_{L,i} \underline{\underline{W}}_i \tilde{\mathcal{K}}^T + \underline{\underline{B}}_{L,i} \underline{\underline{W}}_i \tag{3b}$$

Since the entries of the compliance matrix are the desired quantities in Eq. (2), this can be recast into a linear system of equations for the entries in the compliance matrix according to

$$\underline{\underline{U}}_i \underline{\underline{G}}^{(j)} \underline{S} = \underline{\epsilon}_i^{(j)} - \underline{\underline{V}}_i \underline{\mathcal{F}}^{(j)} \tag{4}$$

where $\underline{S}$ is a 36×1 column vector of the compliance matrix entries and $\underline{\underline{G}}^{(j)}$ is a 6×36 matrix containing entries from the stress resultants defined by

$$\underline{S}^T = \{S_{11}, S_{12}, \cdots S_{16}, S_{21}, \cdots, S_{65}, S_{66}\} \tag{5a}$$

$$\underline{\underline{G}}^{(j)} = \begin{bmatrix} \underline{\mathcal{F}}^{(j)T} & \underline{0} & \underline{0} & \underline{0} & \underline{0} & \underline{0} \\ \underline{0} & \underline{\mathcal{F}}^{(j)T} & \underline{0} & \underline{0} & \underline{0} & \underline{0} \\ \underline{0} & \underline{0} & \underline{\mathcal{F}}^{(j)T} & \underline{0} & \underline{0} & \underline{0} \\ \underline{0} & \underline{0} & \underline{0} & \underline{\mathcal{F}}^{(j)T} & \underline{0} & \underline{0} \\ \underline{0} & \underline{0} & \underline{0} & \underline{0} & \underline{\mathcal{F}}^{(j)T} & \underline{0} \\ \underline{0} & \underline{0} & \underline{0} & \underline{0} & \underline{0} & \underline{\mathcal{F}}^{(j)T} \end{bmatrix} \tag{5b}$$

with $\underline{0}$ being a 1×6 vector of zeros.

Eq. (4) provides a system of six equations for the 36 unknown compliance coefficients, resulting in an underdetermined system of equations. Moreover, since the last three rows of $\underline{\underline{U}}_i$ are all null, only three of the equations are non-trivial and are only dependent on the out-of-plane strain components, ϵ_{11}, ϵ_{12}, and ϵ_{13} . Thus, to obtain a unique solution, the out-of-plane strain components must be evaluated under six independent loads and at two or more points on the cross-section. Combining the equations under multiple loads and at multiple points around the cross-sectional leads to a final system of equations of the form

$$\text{(6)} \qquad \begin{Bmatrix} \underline{\underline{U}}_1\underline{\underline{G}}^{(1)} \\ \vdots \\ \underline{\underline{U}}_N\underline{\underline{G}}^{(1)} \\ \underline{\underline{U}}_1\underline{\underline{G}}^{(2)} \\ \vdots \\ \underline{\underline{U}}_N\underline{\underline{G}}^{(2)} \\ \underline{\underline{U}}_1\underline{\underline{G}}^{(L)} \\ \vdots \\ \underline{\underline{U}}_N\underline{\underline{G}}^{(L)} \end{Bmatrix} \underline{S} = \begin{Bmatrix} \underline{\epsilon}_1^{(1)} \\ \vdots \\ \underline{\epsilon}_N^{(1)} \\ \underline{\epsilon}_1^{(2)} \\ \vdots \\ \underline{\epsilon}_N^{(2)} \\ \underline{\epsilon}_1^{(L)} \\ \vdots \\ \underline{\epsilon}_N^{(L)} \end{Bmatrix} - \begin{Bmatrix} \underline{\underline{V}}_1\underline{\mathcal{F}}^{(1)} \\ \vdots \\ \underline{\underline{V}}_N\underline{\mathcal{F}}^{(1)} \\ \underline{\underline{V}}_1\underline{\mathcal{F}}^{(2)} \\ \vdots \\ \underline{\underline{V}}_N\underline{\mathcal{F}}^{(2)} \\ \underline{\underline{V}}_1\underline{\mathcal{F}}^{(L)} \\ \vdots \\ \underline{\underline{V}}_N\underline{\mathcal{F}}^{(L)} \end{Bmatrix}$$

which can be recast in a compact form as

$$\text{(7)} \qquad \underline{\underline{\mathbb{H}}}\underline{S} = \underline{\mathbb{E}} - \underline{\mathbb{V}}$$

for N discrete strain measurements around the cross-section and L loading cases.

3.3. Stiffness matrix calculation

In Eq. (6), matrix $\underline{\underline{V}}_i$ depends on the warping field, $\underline{\underline{W}}$, and strain interpolation matrices, $\underline{\underline{A}}_L$ and $\underline{\underline{B}}_L$, which requires a finite element or numerical model of the cross-section to evaluate. Specifically, the strain interpolation matrices must be evaluated for the local element containing the location where the strain is measured, while the warping field, which depends on both the geometry and material properties, must be calculated using the finite element model of the entire cross-section.

The strains, $\underline{\epsilon}$, are determined experimentally using DIC for six independent sets of sectional forces, $\underline{\mathcal{F}}$. The DIC algorithm provides data for hundreds of points, N, on the external surface of a given cross-section, which leads to a highly overdetermined system for the sectional compliance matrix entries, $\underline{S}$, in Eq. (6). This system is then solved using a singular value decomposition, which helps average out any anomalous data in the DIC measurements. Once the individual compliance matrix entries have been calculated, the actual compliance matrix can be reconstructed as

$$\text{(8)} \qquad \underline{\underline{S}} = \begin{bmatrix} S_{11} & S_{12} & S_{13} & S_{14} & S_{15} & S_{16} \\ S_{21} & S_{22} & S_{23} & S_{24} & S_{25} & S_{26} \\ S_{31} & S_{32} & S_{33} & S_{34} & S_{35} & S_{36} \\ S_{41} & S_{42} & S_{43} & S_{44} & S_{45} & S_{46} \\ S_{51} & S_{52} & S_{53} & S_{54} & S_{55} & S_{56} \\ S_{61} & S_{62} & S_{63} & S_{64} & S_{65} & S_{66} \end{bmatrix}$$

The compliance matrix should be symmetric (i.e. S_{ij} = S_{ji}); however, errors in the experimental measurements of both the strain and force can lead to asymmetries in the matrix. Therefore, the following two conditions are applied to eliminate any substantial asymmetries resulting from measurement error

$$\text{(9a)} \qquad \text{if } sgn(S_{ij}) \neq sgn(S_{ji}) \qquad \text{then} \quad S_{ij} = S_{ji} = 0$$

$$\text{(9b)} \qquad \text{if } \left|\frac{S_{ij}}{S_{ji}}\right| > 2 \text{ or } \left|\frac{S_{ji}}{S_{ij}}\right| > 2 \qquad \text{then} \quad S_{ij} = S_{ji} = 0$$

where the first condition eliminates terms of opposite signs and the second condition eliminates terms of sufficiently different magnitudes.

The stiffness matrix, $\underline{\underline{K}}$, is then computed as the inverse of the compliance matrix and defined by

$$\text{(10)} \qquad \underline{\underline{K}} = \underline{\underline{S}}^{(-1)} = \begin{bmatrix} K_{11} & K_{12} & K_{13} & K_{14} & K_{15} & K_{16} \\ K_{21} & K_{22} & K_{23} & K_{24} & K_{25} & K_{26} \\ K_{31} & K_{32} & K_{33} & K_{34} & K_{35} & K_{36} \\ K_{41} & K_{42} & K_{43} & K_{44} & K_{45} & K_{46} \\ K_{51} & K_{52} & K_{53} & K_{54} & K_{55} & K_{56} \\ K_{61} & K_{62} & K_{63} & K_{64} & K_{65} & K_{66} \end{bmatrix}$$

where indices 1, 2, 3, 4, 5, and 6 indicate extension, lag shear, flap shear, torsion, flap bending, and lag bending, respectively. In a more compact notation, the stiffness matrix can be written as

$$\text{(11)} \qquad \underline{\underline{K}} = \begin{bmatrix} \underline{\underline{K}}_F & \underline{\underline{K}}_{FM} \\ \underline{\underline{K}}_{FM}^T & \underline{\underline{K}}_M \end{bmatrix}$$

where $\underline{\underline{K}}_F$, $\underline{\underline{K}}_{FM}$, and $\underline{\underline{K}}_M$ are all 3 × 3 matrices, with units of N (lb), N-m (lb-in), and N-m^2 (lb-in^2), respectively.

4. EXPERIMENTAL PROCEDURE

All the experiments were performed using a custom test frame at the University of Maryland. In this section, the test stand and articles are described, as well as the DIC measurement set up.

4.1. Test Articles

To verify the calculation procedure for the stiffness matrix, three sets of test articles are considered: an isotropic beam, a composite beam presenting bending-torsion coupling, and a composite blade. For the isotropic test article, an aluminum beam with a rectangular cross-section was manufactured. The beam was made of 6061-T6 aluminum, with a Young's Modulus of E = 68.9 GPa (1.00 × 10^7 lb/in^2) and Poisson's ratio of ν = 0.33. The beam was nominally 73.7 cm (29 in.) long with cross-sectional width of w = 10.2 cm (4 in) and a thickness of t = 0.476 cm (0.188 in.). To ensure that the calculation procedure was repeatable, three separate beams were manufactured and tested, with the measured geometric details summarized in Table 1.

A composite beam was next manufactured in-house using PYROFIL$^{\text{TM}}$ TR50S 12K uni-directional prepreg. The beam was nominally 71.1 cm (28 in.) long with cross-sectional width of w = 7.62 cm (3 in) and thickness of t = 0.244 cm (0.096 in.). A ply sequence of $[-30^\circ_2/90^\circ_2/-45^\circ_2/0^\circ_2]_s$ was used to provide a significant bending-torsion coupling. To fabricate the beams, a simple mold consisting of two 2.54 cm (1 in) plates was used, with the bottom plate containing a 71.76 cm (28.25 in.) by 8.00 cm (3.15 in.) cutout to a depth of 0.244 cm (0.096 in.). The 16 prepreg layers were then cut from the uni-directional prepreg and laid-up at the desired angles, with a release film wrapped around

Table 1: Measured geometric properties of the aluminum test articles.

Parameter		Beam 1	Beam 2	Beam 3
Length, l	(cm)	73.61	73.61	73.58
	(in)	28.98	28.98	28.97
Width, w	(cm)	10.30	10.27	10.24
	(in)	4.055	4.045	4.030
Thickness, t	(cm)	0.489	0.488	0.489
	(in)	0.193	0.192	0.193

the outside to facilitate release of the cured beam from the mold, with the main components shown in Fig. 1. The mold was then sealed using 16 bolts along the outer edge of the mold and cured in a mechanical convection oven, by heating the oven up to 135°C (275°F), holding for 90 minutes, and then cooling. Based on this cure cycle, the average material properties provided by the vendor for the cured prepreg have Young's moduli of $E_1 = 130$ GPa (1.89×10^7 lb/in^2) and $E_2 = 8.68$ GPa (1.26×10^6 lb/in^2), Poisson's ratios of $\nu_{12} = 0.28$ and $\nu_{23} = 0.33$, and shear modulus of $G_{12} = 4.60$ GPa (5.22×10^5 lb/in^2) .[11] The final geometry was then machined from the cured beam, resulting in dimensions of $l = 70.9$ cm (27.9 in.), $w = 7.62$ cm (3.00 in.), and $t = 0.244$ cm (0.096 in.).

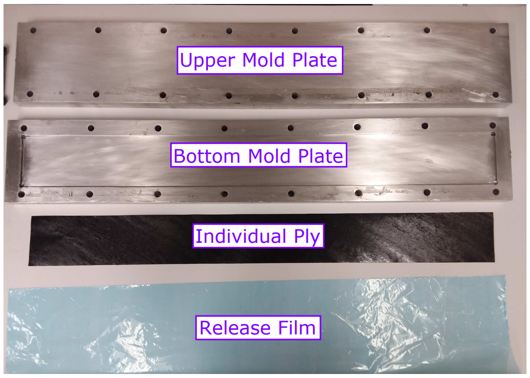

Fig. 1: Components used for fabrication of the composite beam

Finally, a 53.3 cm (21 in.) composite blade was manufactured in-house using a VR-7 airfoil profile with a 8.00 cm (3.15 in.) chord, with the main components highlighted in Fig. 2. The blade structure consisted of a single layer of HEXPLY®8552 SGP196-PW prepreg, oriented at 45°, wrapped around a core of ROHACELL®IG-F 31 foam. A layer of Cytec FM®300 film adhesive was included between the prepreg and foam core to prevent the resin from bleeding into the foam. A d-shaped spar, consisting of an additional ply of the prepreg wrapped around an aluminum 6061 core, was incorporated along the first and last 5.61 cm (2.21 in.) of the span for the purposes of applying the load to the blade and clamping the blade in the test stand. The main components were then wrapped with a release film, placed inside a mold with a VR-7 airfoil cutout and cured in an oven, by heating the oven up to 177° (350°F), holding for 150 minutes, and then cooling. Based on this cure cycle, the average material properties provided by the vendor for the cured prepreg have Young's moduli of $E_1 = 84.8$ GPa (1.23×10^7 lb/in^2) and $E_2 = 79.9$ GPa (1.16×10^7 lb/in^2), Poisson's ratios of $\nu_{12} = 0.30$ and $\nu_{23} = 0.34$, and shear modulus of $G_{12} = 5.60$ GPa (8.12×10^5 lb/in^2) .[12] The final manufactured blade is shown in Fig. 3.

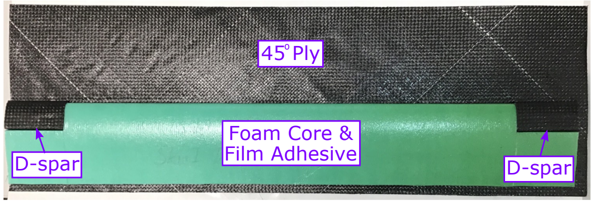

Fig. 2: Main components used for fabriacation of the composite blade

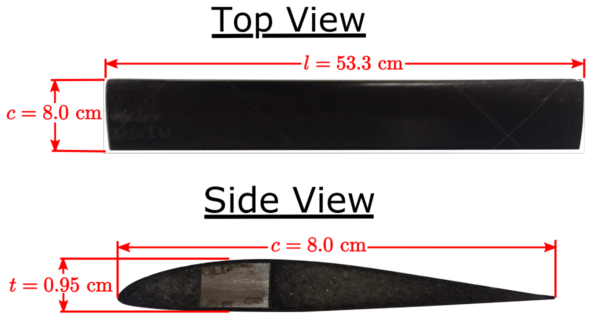

Fig. 3: Manufactured composite blade

4.2. Test Stand

One of the main requirements for uniquely identifying all the entries of the compliance and stiffness matrices is to measure the strains under six linearly independent loads. In order to apply these loads, a custom test stand was built at the University of Maryland as shown in Fig. 4, with the main structure consisting of an 80/20 frame. An ATI Omega 160 force/torque sensor was mounted at the base of the structure to measure the applied forces and moments. The force sensor was calibrated for loads up to 2500 N (562 lb) in the flap and lag directions (F_y and F_z) and 6250 N (1405 lb) in the axial direction (F_x) and for moments up to 400 N-m (3540 lb-in) in all three directions. The test articles were secured to the load cell by clamping the article between two 20.3 cm (8 in.) × 5.08 cm (2 in.) × 1.91 cm (0.75 in.) 7075 aluminum bars, with individual spacers machined to conform to the cross-sectional geometry in order to provide a uniform clamp.

The loading is then applied at the tip of the test articles, with hanging weights used to apply small loads and winches used to apply larger loads. To generate the desired sets of forces and moments, a system of pulleys is used to redirect the loads, which are all initially applied in the vertical (axial) direction. A set of aluminum bars, similar to those used to clamp the blade to the load cell, are attached to the tip of the article, which provide an additional moment arm for torque and bending moment applications.

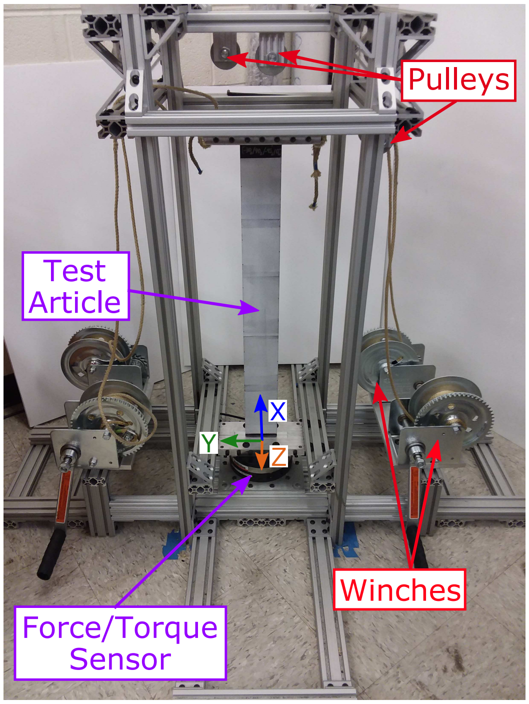

Fig. 4: Test stand for applying loads to test articles

4.3. DIC Measurement Setup

The strain field on the surface of the test articles was measured using the digital image correlation (DIC) technique, with the setup shown in Fig. 5. The present study used two stereoscopic cameras (Basler acA2440-75um with Schneider Xenoplan 28 mm lenses) to obtain images of the test articles, both when no load is applied (reference image) and under the desired loads, with two high-intensity LED arrays (Visual Instrumentation Corp Model 901000H) used to illuminate the test articles. The two cameras were mounted on a tripod and oriented at approximately 20° inwards from the flap direction to obtain 3-D measurements. An adjustable center column on the tripod allowed for 20.3 cm (8 in.) of vertical travel of the camera system during testing, ensuring that data could be collected along a significant portion of the span of the test articles.

An important step in the DIC measurement is the surface preparation of the test articles. To obtain an accurate strain measurement, the surface of the test article must have a high-intensity stochastic pattern with the same deformation as the surface. In order to achieve this pattern, all test articles were first sanded and wiped down with a damp lint-free cloth to remove all debris from the surface. The surfaces were then spray painted with a matte white paint, with the matte finish required to eliminate any potential glare from the LED array. Finally, the stochastic pattern was generated using a stamp with a random dot pattern and black ink, with images of the initially manufactured and prepared composite beam shown in Fig. 6. Since the cameras only capture a subset of the full span of the test article during any single image, additional markings (letters) are placed at every inch along the span to provide knowledge of the exact spanwise locations currently being captured during testing.

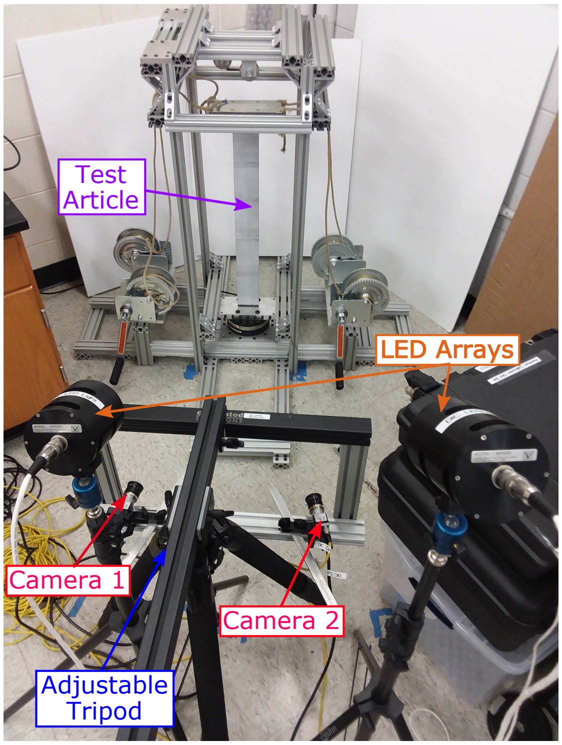

Fig. 5: DIC system measurement setup

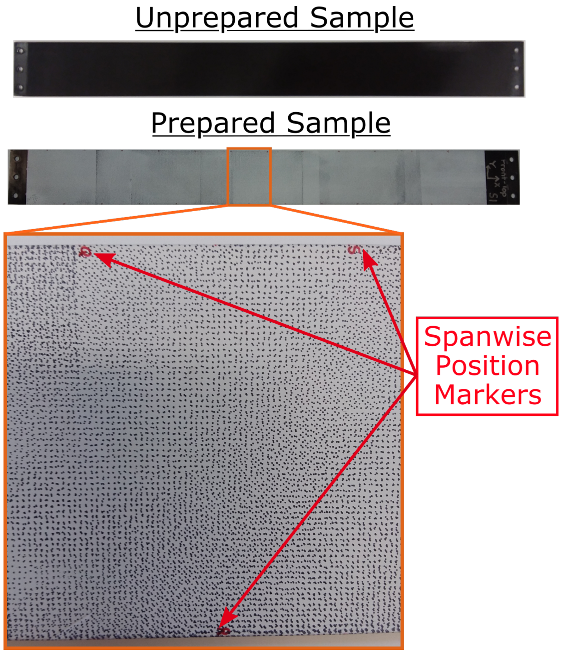

Fig. 6: Test article before and after random speckle pattern is applied

4.4. Image processing

After capturing images of the test articles in both the deformed and undeformed configurations, the DIC software (VIC 3D from Correlated Solutions) was used to calculate the 3-D deformation and strain fields. The cameras are set up to capture a 24 cm (9.4 in.) × 24 cm (9.4 in.) field of view near the test article with an image size of 2488 × 2488 pixels. An area of interest encompassing 20.3 cm (8 in.) along the span is then defined in the software, using the markings on the blade, which defines the region of the image where data should be calculated. The software then divides the area of interest into smaller subsets of 29 × 29 pixels for calculating the displacement field with a 7 pixel step used to map the individual subset to the full region. This results in displacement measurements at every 0.80 mm (0.031 in.) along the span and chord.

During testing 10 separate images are collected at 1.5 second intervals for each loading condition and then averaged together to smooth out any anomalous data points obtained during the image processing. This averaging also helps provide a means of estimating the accuracy of the strain measurement, particularly by considering the non-zero strains obtained when averaging the 10 images corresponding to the undeformed reference state. Across all tests, the reference state was found to have a mean strain of less than $\pm 10\mu\epsilon$ with standard deviations of less than 15 $\mu\epsilon$.

The strain field is calculated in the DIC software by subdividing the collected dataset into three-noded triangular elements and then numerically differentiating the displacements, similar to a conventional finite element method. The key parameter used to control the accuracy and smoothness of this strain data is the filter size. Having too small of a filter size can result in unexpected jumps in strain between neighboring points; however, having too large of a filter size can result in an over-smoothing of the data thus eliminating expected strain variations and concentrations. From simple testing of aluminum beams under a flapwise shear, it was found that a filter size of 45 ensured that the measured strains were within 2.5% of the analytically calculated strain values, while also avoiding excessive smoothing of the data.

From the DIC algorithm, the calculated strain components are ϵ_{11}, ϵ_{12}, and ϵ_{22}, while the stiffness matrix calculation procedure requires the three out-of-plane components ϵ_{11}, ϵ_{12}, and ϵ_{13}. The non-measured component, ϵ_{13}, can be calculated using the constitutive equations and local equilibrium equations; however, the additional cost required to calculate ϵ_{13} from the measured data did not add any accuracy in the calculated stiffness matrices and the equations corresponding to ϵ_{13} were therefore ignored in the current analysis.

4.5. Test Envelope

For the aluminum beam, the test envelope of loads and maximum expected strains is summarized in Table 2. For all but the axial load case, both a positive and negative load were applied to provide a redundant set of data. In the axial load case, the maximum achievable load was limited by the saturation limit of the load cell. A compressive (negative) load was not applied, as the buckling limit was estimated at about 330 N (75 lb), which would only produce a maximum expected strain of 9 $\mu\epsilon$. For both the lag shear and lag bending loads, the maximum load was limited by a local buckling instability that occurred near the mid-span at an applied load near 500 N-m. For both the flap shear and flap bending loads, the maximum load was limited by the large deflections that started to bring the upper portion of the beam out of focus in the camera. For the torsional load, no specific limitations were observed, and the load was selected to achieve a desirable strain of about 2500 $\mu\epsilon$. In order to closely approximate pure torsional and bending moments, force couples were applied at the tip of the specimen according to Fig. 7. For the flap and lag bending moments, the four winches were used to produce the four necessary loads. For the torsional moment, two sets of hanging weights were used to produce the force couple.

Table 2: Applied tip loads for the aluminum test articles.

Test #	Load case	Applied Tip Load	Expected Strain, max $\{\lvert\epsilon\rvert\}$
1	Axial	$F_x = +6250$ N	187 $\mu\epsilon$
2,3	Lag Shear	$F_y = \pm 670$ N	740 $\mu\epsilon$
4,5	Flap Shear	$F_z = \pm 89$ N	2200 $\mu\epsilon$
6,7	Torsion	$M_x = \pm 46$ N-m	2378 $\mu\epsilon$
8,9	Flap Bending	$M_y = \pm 52$ N-m	1967 $\mu\epsilon$
10,11	Lag Bending	$M_z = \pm 450$ N-m	778 $\mu\epsilon$

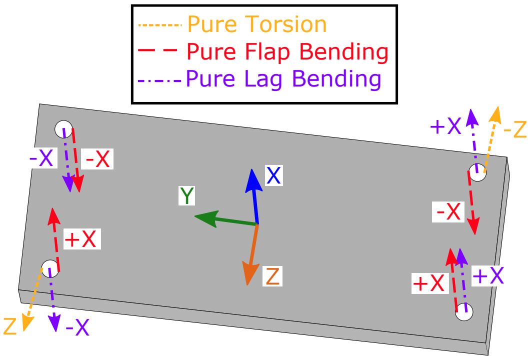

Fig. 7: Schematic for applying pure bending and torsional moments

For the composite beam, the test envelope of loads and maximum expected strains is summarized in Table 3. Tests were again run for 11 different load cases, with the negative load neglected for the axial load case due to buckling concerns. Two main constraints arose due to the torsion/flap bending coupling. First, the beam was very unstable when subjected to a lagwise shear/bending. This meant that in order to apply both the lag shear and lag bending loads, a net axial force also needed to be applied to reduce this instability, as highlighted in the specified loads for tests 2 and 3 as well as 10 and 11. Second, the beam experienced both a twist and flapwise motion when subjected to a flap bending or torsional moment. Therefore, the flap shear load resulted in a variation of both flap bending and torsional moment along the span.

For the composite blade, the test envelope of loads and maximum expected strains is summarized in Table 4. In addition to the negative axial load being neglected during testing, the negative lag shear (F_y) was also not applied, due to concerns about high compressive loads leading to possible local buckling in the trailing edge. No additional limitations were expected during testing and the remaining loads were selected

Table 3: Applied tip loads for the composite beam.

Test #	Load case	Applied Tip Load	Expected Strain, max $\{\lvert\epsilon\rvert\}$
1	Axial	$F_x = +6250$ N	635 $\mu\epsilon$
2,3	Lag Shear	$F_x = 5300$ N $F_y = \pm 725$ N	844 $\mu\epsilon$
4,5	Flap Shear	$F_z = \pm 3.9$ N	1396 $\mu\epsilon$
6,7	Torsion	$M_x = \pm 2.9$ N-m	1958 $\mu\epsilon$
8,9	Flap Bending	$M_y = \pm 2.0$ N-m	1154 $\mu\epsilon$
10,11	Lag Bending	$F_x = 4500$ N $M_z = \pm 160$ N-m	1665 $\mu\epsilon$

to provide maximum strains between 2000 $\mu\epsilon$ and 4000 $\mu\epsilon$, in order to maximize the signal to noise ratio in the strain measurements while minimizing the risk of structural failures in the blade.

Table 4: Applied tip loads for the composite blade.

Test #	Load case	Applied Tip Load	Expected Strain, max $\{\lvert\epsilon\rvert\}$
1	Axial	$F_x = +1550$ N	3610 $\mu\epsilon$
2	Lag Shear	$F_y = \pm 67$ N	3428 $\mu\epsilon$
3,4	Flap Shear	$F_z = \pm 7.9$ N	2640 $\mu\epsilon$
5,6	Torsion	$M_x = \pm 8.2$ N-m	3059 $\mu\epsilon$
7,8	Flap Bending	$M_y = \pm 3.9$ N-m	2825 $\mu\epsilon$
9,10	Lag Bending	$M_z = \pm 23$ N-m	2712 $\mu\epsilon$

During testing of any test article, an individual image could provide strain data along 20.3 cm (8 in.) of the span. Since the camera system was able to traverse an additional 20.3 cm (8 in.), multiple images were collected during a single test to allow data to be collected over a maximum range of 40.6 (16 in.) along the span. However, data tended to have the lowest signal to noise ratios within 0.25 cm (0.1 in.) of the spanwise boundaries, primarily due to the fact that less data was available in these regions for numerical differentiation and smoothing, and strain data was only extracted from the middle 19.1 cm (7.5 in.) of the image. To maximize the amount of strain data measured along the span, images were collected at three spanwise locations, denoted by image sets 1, 2, and 3. Image set 1 ranged from 8.26 cm (3.25 in.) to 27.3 cm (10.75 in.) along the span, image set 2 ranged from 18.4 cm (7.25 in.) to 37.5 cm (14.75 in.) along the span, and image set 3 ranged from 28.6 cm (11.25 in.) to 47.6 cm (18.75 in.) along the span, which provided data over a total of 39.4 cm (15.5 in.). For each image set, the 10 images for averaging out anomalous points were collected in both the deformed and undeformed configuration, resulting in a total of 60 images collected during a single test. In locations where the image sets overlapped, the strain fields were averaged together to provide a more continuous profile along the span.

5. RESULTS

5.1. Aluminum Beam

The experimentally measured stiffness matrices for the three aluminum beams are examined in this section. Figures 8-10 show the axial (ϵ_{11}), chordwise (ϵ_{22}), and shear (ϵ_{12}) strains, respectively, as measured by the DIC system for 18.4 cm (46.7 in.) to 37.5 cm (95.3 in.) along the span, when the aluminum beam is subjected to a negative flap bending load (load test #9). For this loading case, the strain should be constant with respect to both the span (x) and the chord (y), with expected strains of ϵ_{11} = -1967 $\mu\epsilon$, ϵ_{22} = 652 $\mu\epsilon$, and ϵ_{12} = 0 $\mu\epsilon$ on the front surface and expected strains of ϵ_{11} = 1967 $\mu\epsilon$, ϵ_{22} = -652 $\mu\epsilon$, and ϵ_{12} = 0 $\mu\epsilon$ on the back surface. The DIC measurements showed great agreement with the expected strains, with average strains of ϵ_{11} = -1948 $\mu\epsilon$, ϵ_{22} = 618 $\mu\epsilon$, and ϵ_{12} = -49.5 $\mu\epsilon$ on the front surface and ϵ_{11} = -1901 $\mu\epsilon$, ϵ_{22} = -555 $\mu\epsilon$, and ϵ_{12} = 12.1 $\mu\epsilon$ on the back surface. In addition, the DIC measurements were mostly constant along both the span and chord, with standard deviations of ϵ_{11} = $\pm 8.1\mu\epsilon$, ϵ_{22} = $\pm 29.7\mu\epsilon$, and ϵ_{12} = $\pm 22.9\mu\epsilon$. The majority of the variations from the expected constant strain occurred near the outer edges of the test articles, which can be easily seen in the shear strain results shown in Fig. 10 where the average strain is much smaller.

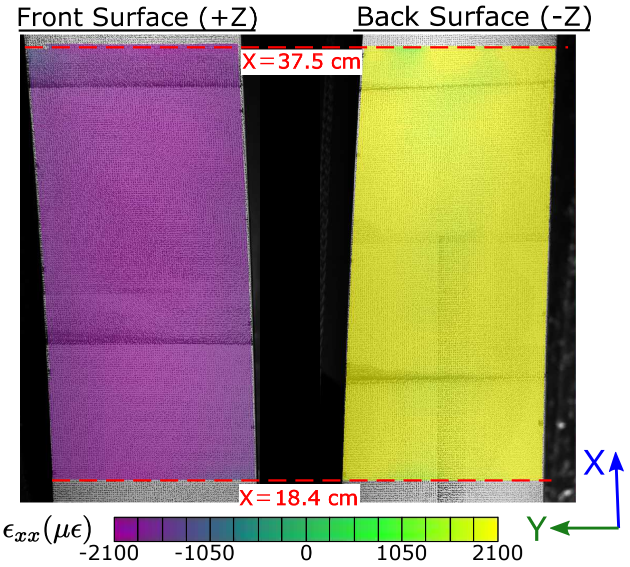

Fig. 8: DIC axial strain (ϵ_{11}) distribution for the aluminum beam under a pure bending of $M_y = -52$ N-m.

Once the DIC software processed the images collected for all 11 load cases, the strains were then extracted for cross-sections (i.e. constant x) at every 0.64 cm (0.25 in.) along the span. The strain and force/moment data for all load cases were then substituted into Eq. (7) and the stiffness matrix entries were calculated at each spanwise location with results shown in Figs. 11-13. For a beam made of an isotropic material with a rectangular cross-section, all six diagonal entries of the stiffness matrix can be evaluated analytically ,[13,14] which were used to non-dimensionalize the results for all

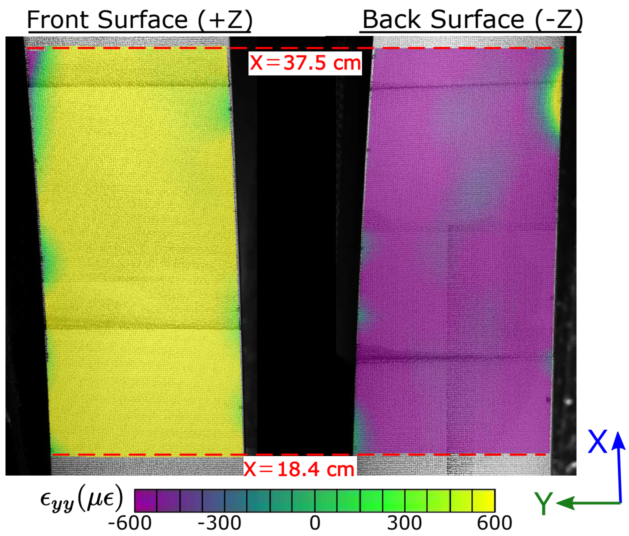

Fig. 9: DIC chordwise strain (ϵ_{22}) distribution for the aluminum beam under a pure bending of $M_y = -52$ N-m.

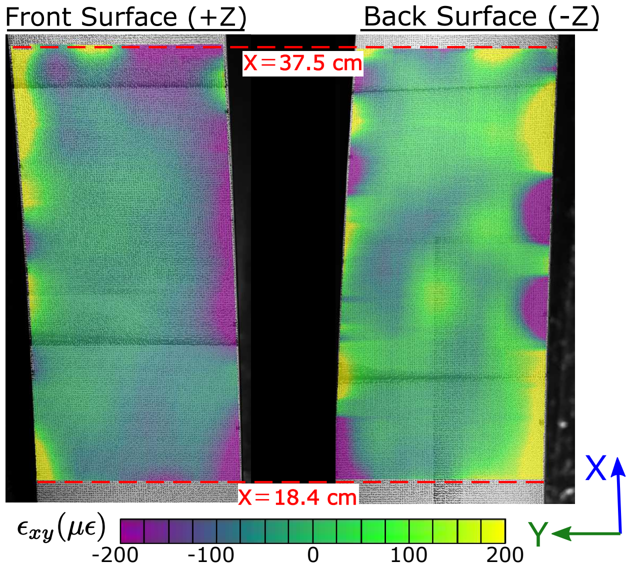

Fig. 10: DIC shear strain (ϵ_{12}) distribution for the aluminum beam under a pure bending of $M_y = -52$ N-m.

three beams. The axial (K_{11}), flap shearing stiffness (K_{33}), torsional stiffness (K_{44}), flap bending stiffness (K_{55}), and lag bending stiffness (K_{66}) had relatively small variations in the measured stiffness values along the span. For all three beams, the measured lag shearing stiffness (K_{22}) was significantly higher than the analytical value closest to the clamp and showed some significant variations along the span for the third test article. When considering the full shear strain distribution provided by the DIC software under the lag shear load, edge effects were observed up until about 20.3 cm (8 in.). In addition, while the lag shear loads produced significant axial strains due to bending, the expected shear strain, the dominant factor for calculating the shear stiffness, was only 83 $\mu\epsilon$, which was only 2-4 times larger than the expected DIC noise levels.

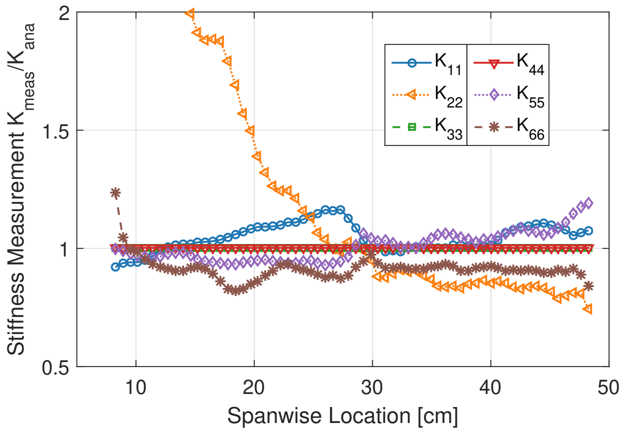

Fig. 11: Variation of the stiffness properties along the span for the first aluminum test article.

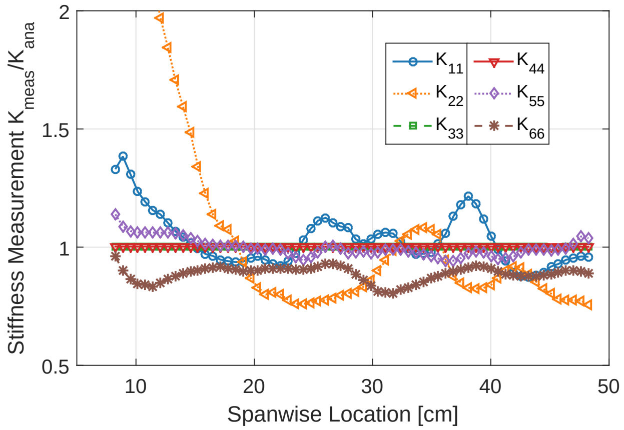

Fig. 12: Variation of the stiffness properties along the span for the second aluminum test article.

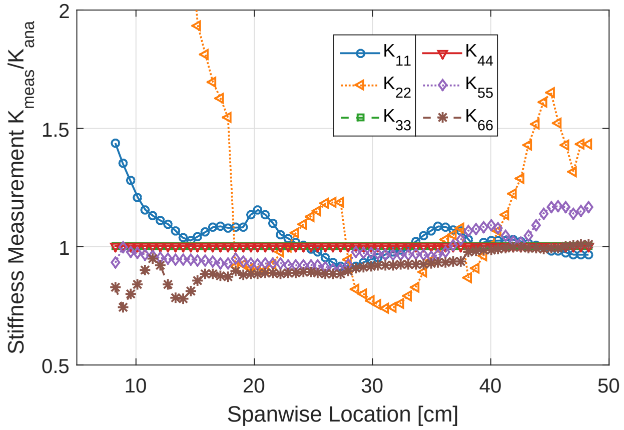

Fig. 13: Variation of the stiffness properties along the span for the third aluminum test article.

The measured dimensional stiffness values for the three beams are compared with the analytically predicted values in Table 5. The stiffness values were averaged along the entire span of the beam with the exception of the lag shear stiffness, which was averaged starting at 20.3 cm (8 in.) to avoid the initial overprediction from the edge effects. Overall, the flap shear stiffness (K_{33}), the torsional stiffness (K_{44}), and the flap bending stiffness (K_{55}) showed excellent agreement with the analytic solutions, with a maximum difference of 1.4%. The experimental measurements for the axial stiffness (K_{11})

and lag bending stiffness (K_{66}) showed good agreement between all three test articles; however, they were overpredicted by at most 5.5% and underpredicted by at most 11%, respectively, when compared to the analytic values. The lag shear stiffness showed the greatest variation between test articles and was also overpredicted by a maximum of 18% for the third test article.

Table 5: Average measured stiffness values of the three aluminum test articles.

Stiffness entry	Analytic	Beam 1	Beam 2	Beam 3
K_{11}, N	3.34×10^7	3.49×10^7	3.44×10^7	3.48×10^7
K_{22}, N	1.05×10^7	1.16×10^7	9.16×10^6	1.23×10^7
K_{33}, N	4.68×10^5	4.72×10^5	4.69×10^5	4.69×10^5
K_{44}, N-m^2	92.1	92.3	92.2	92.3
K_{55}, N-m^2	63.1	63.6	62.2	63.1
K_{66}, N-m^2	2.87×10^4	2.63×10^4	2.55×10^4	2.63×10^4

5.2. Composite Beam

The experimentally measured stiffness matrix for the composite beam is examined in this section. Figures 14-16 show the axial (ϵ_{11}), chordwise (ϵ_{22}), and shear (ϵ_{12}) strains, respectively, as measured by the DIC system for 8.26 cm (3.25 in.) to 27.3 cm (10.75 in.) along the span, when the composite beam is subjected to an axial load combined with a negative lag bending moment (load test #11). Under this load, the strain should vary linearly along the width of the beam and remain constant along the span, which is well captured in the experimental DIC measurements. The expected strains, calculated from the *SectionBuilder* model, along the left side of the beam ($+y$) are ϵ_{11} = 1920 $\mu\epsilon$, ϵ_{22} = -430 $\mu\epsilon$, and ϵ_{12} = 1853 $\mu\epsilon$ and along the right side of the beam ($-y$) are ϵ_{11} = -888 $\mu\epsilon$, ϵ_{22} = 107 $\mu\epsilon$, and ϵ_{12} = -864 $\mu\epsilon$. The DIC measurements had average strains of ϵ_{11} = 2089 $\mu\epsilon$, ϵ_{22} = -476 $\mu\epsilon$, and ϵ_{12} = 1807 $\mu\epsilon$ along the left edge and ϵ_{11} = -911 $\mu\epsilon$, ϵ_{22} = 97.5 $\mu\epsilon$, and ϵ_{12} = -936 $\mu\epsilon$ along the right edge, which were mostly higher than the expected strains. Throughout all test cases, the measured strains were on average 5 to 10% higher than the expected strains.

After the DIC software processed the images collected for all 11 load cases, the strains were again extracted for cross-sections at every 0.64 cm (0.25 in.) from 8.26 cm (3.25 in.) to 47.6 cm (18.75 in.) along the span. The measured strain and force/moment data was then used along with the numerical model to calculate the stiffness matrix entries at each spanwise location using Eq. (7). The measured stiffness values were normalized by the predicted values from the numerical model, with results shown in Fig. 17. Similar to the isotropic beams, the measured lag shearing stiffness, K_{22}, was significantly higher than the predicted value near the clamp due to edge effects in the strain distribution. The lag shearing stiffness also showed the greatest amount of variation along the span, as a result of having the lowest signal to noise ratio. When subjected to the flap bending and flap shear loads, the beam had large tip deflections of approximately 23 cm (9.1 in.), resulting in the upper portion of the beam nearing the limits of the camera focal planes. This introduced additional noise into the strain measurements closer to the tip of the beam, which can be seen by the variations near the upper boundary of the measurement range for the torsion, flap bending, and flap/torsion coupled stiffness terms, K_{44}, K_{55}, and K_{45}, respectively.

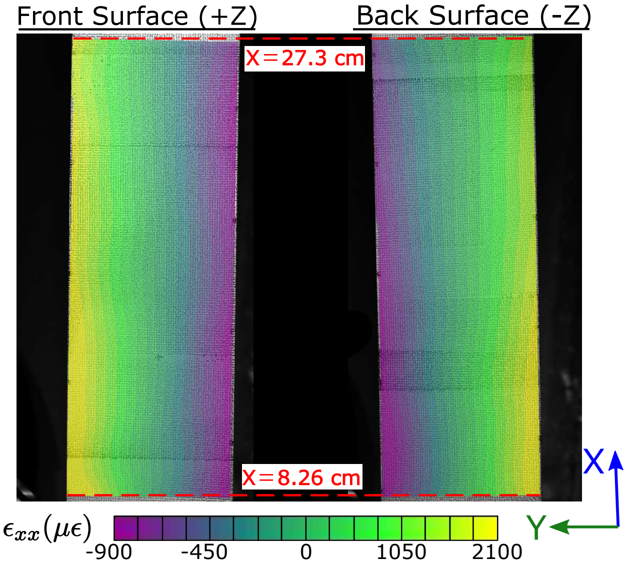

Fig. 14: DIC axial strain (ϵ_{11}) distribution for the composite beam under a combined extension of $F_x = 4500$ N and bending of $M_z = -160$ N-m.

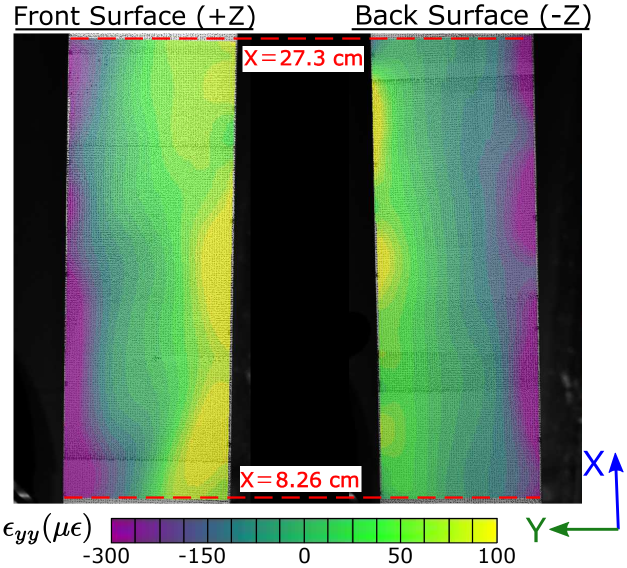

Fig. 15: DIC chordwise strain (ϵ_{22}) distribution for the composite beam under a combined extension of $F_x = 4500$ N and bending of $M_z = -160$ N-m.

From Fig. 17, it was observed that most of the numerical stiffness values were overpredicted compared to the measured values. When manufacturing beams with composite materials, it is not uncommon to see differences between the actual

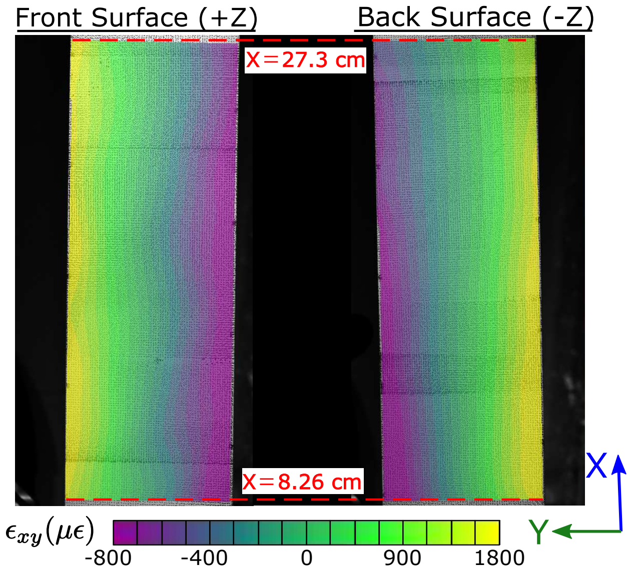

Fig. 16: DIC shear strain (ϵ_{12}) distribution for the composite beam under a combined extension of $F_x = 4500$ N and bending of $M_z = -160$ N-m.

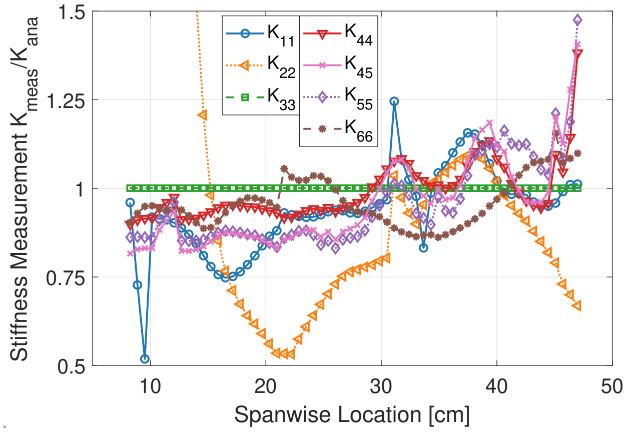

Fig. 17: Variation of the stiffness properties along the span for the composite beam.

material properties and their reported average values, due to variations in both the material itself and the manufacturing process. Many resources, such as the Composite Materials Handbook,[15] show that typical variations between the extrema of the measured values and the mean values can be up to 10 or even 15%. Because the current technique combines experimental data and a numerical model of the cross-section, the selected material properties can impact both the predicted and measured stiffness matrices. Therefore, to consider the potential impact of material properties on the measured stiffness matrices, both the mean properties reported by the vendor and the properties with the Young's moduli and shear modulus reduced by 10% were considered.

Table 6 shows the comparison of the predicted and measured stiffness matrices for the two different sets of material properties. While the measurements were not able to capture the coupling between the extension and lag shear, the remaining seven entries were observed. The measured values for the axial, flap bending, and lag bending stiffnesses, K_{11}, K_{55}, and K_{66}, respectively, remain nearly constant with respect to the material properties used in the numerical model. However, the measured values for the lag shear, flap shear, torsion, and flap/torsion coupled stiffness entries are all reduced when the material properties are reduced, which shows that the experimental measurements and numerical model are coupled for these terms. This behavior indicates that the warping field, the term in the calculation procedure that depends on the material properties, plays a significant role in the shear and torsion behavior, but has a very minor impact on the axial and bending behavior. When using the mean material properties, the numerical stiffness values for the axial, flap bending, and lag bending stiffness are overpredicted by 6.5%, 2.4%, and 3.7%, respectively. With the material properties reduced by 10%, the numerical stiffness values for the axial, flap bending, and lag bending stiffness are underpredicted by 4.0%, 8.0%, and 6.7%, respectively. This suggests that the material properties of the actual manufactured beam are between 90 and 100% of their mean values.

Table 6: Comparison of average composite beam stiffness values.

Stiffness entry	Mean material properties		10% reduced properties	
	Numerical	Measured	Numerical	Measured
K_{11}, N	1.06×10^7	9.96×10^6	9.57×10^6	9.97×10^6
K_{12}, N	2.06×10^6	−	1.85×10^6	−
K_{22}, N	2.19×10^6	2.09×10^6	1.97×10^6	1.93×10^6
K_{33}, N	4.04×10^3	4.03×10^3	3.63×10^3	3.64×10^3
K_{44}, N-m^2	6.33	6.38	5.70	5.75
K_{45}, N-m^2	3.88	3.71	3.49	3.55
K_{55}, N-m^2	4.33	4.23	3.89	4.23
K_{66}, N-m^2	4.19×10^3	4.04×10^3	3.77×10^3	4.04×10^3

5.3. Composite Blade

The experimentally measured stiffness matrix for the composite blade is examined in this section. Figures 18-20 show the axial (ϵ_{11}), chordwise (ϵ_{22}), and shear (ϵ_{12}) strains, respectively, as measured by the DIC system for 26.0 cm (10.25 in.) to 45.1 cm (17.75 in.) along the span, when the blade is subject to a positive flap shear load (load test #3). Under this load, the maximum and minimum axial strains should occur at $0.31c$ and $0.34c$ on the front and back surfaces, respectively, and decrease linearly along the span. Since a constant shear force is being applied, the shear strain should have little variation along the span but should vary along the chord. On the front surface, the shear strain is expected to have a maximum strain of 93 $\mu\epsilon$ and minimum strain of -161 $\mu\epsilon$, transitioning from a positive to negative strain at $0.32c$. On the back surface, the shear strain is expected to have a maximum strain of 102 $\mu\epsilon$ and minimum strain of -73 $\mu\epsilon$, transitioning from a negative to positive shear strain at $0.26c$. With exception to a few localized strain distributions near the leading and trailing edges, the DIC measurements under the flap shear load showed good correlation with expected strain distributions. Similar levels of agreement were observed between the DIC measurements and predicted strain distributions for the remaining tests, although the measured strains were generally slightly larger than the predicted strains.

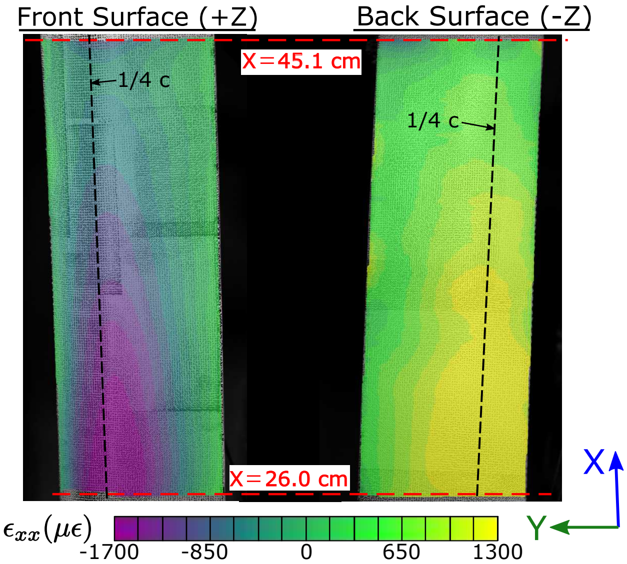

Fig. 18: DIC axial strain (ϵ_{11}) distribution for the composite blade under a flap shear of $F_y = 7.9$ N.

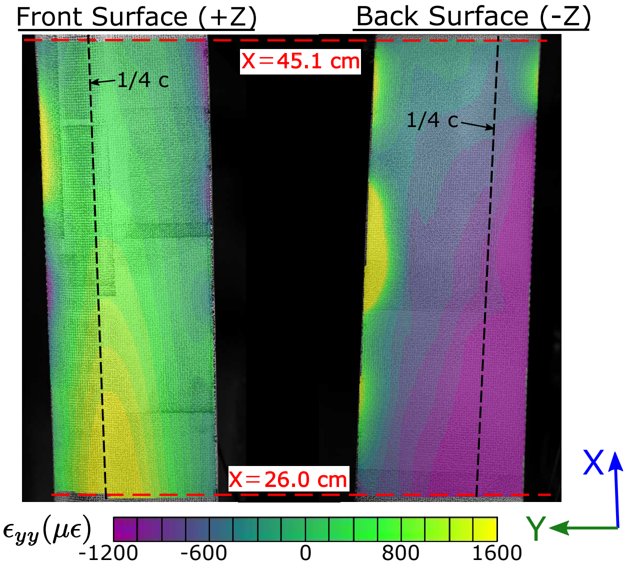

Fig. 19: DIC chordwise strain (ϵ_{22}) distribution for the composite blade under a flap shear of $F_y = 7.9$ N.

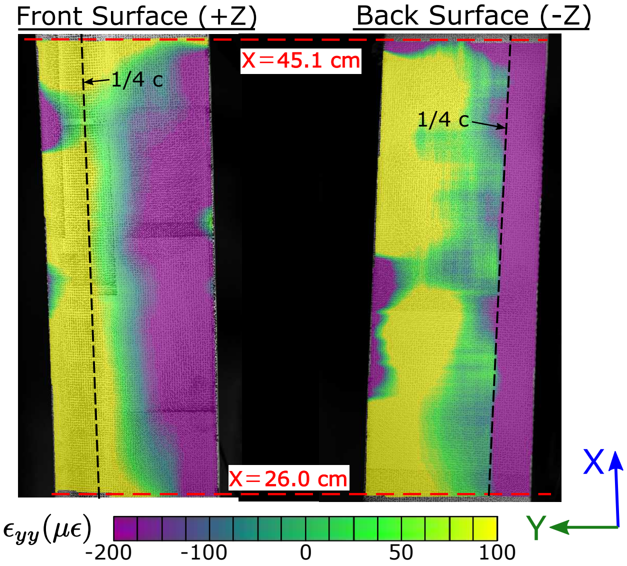

Fig. 20: DIC shear strain (ϵ_{12}) distribution for the composite blade under a flap shear of $F_y = 7.9$ N.

Since the composite blade had a shorter overall length compared to the other test articles, the strains were only able to be measured from 8.26 cm (3.25 in.) to 45.1 cm (17.75 in.) along the span, with the data extracted for cross-sections at every 0.64 cm (0.25 in.). When attached to the test stand, the force data was measured at $0.597c$, and the stiffness matrix was then calculated with respect to this chordwise location using Eq. 7. The normalized spanwise distributions of the stiffness matrix entries are shown in Figs. 21 - 22, for the diagonal and off-diagonal terms, respectively. From Fig. 21, it can be seen that all six values for the measured diagonal stiffness entries were below their predicted values, indicating that the material properties used in the numerical model were likely higher than the actual material properties. The measured properties were also fairly constant along the majority of the blade's span, with the largest variations exhibited closest to the blade root and tip. From Fig. 22, it was observed that six off-diagonal stiffness terms were present. The three terms coupling the axial and bending behavior, K_{15}, K_{16}, and K_{56}, indicate that the selected coordinate system is not at the centroid of the cross-section and these terms can be used to determine both the centroid and the orientation of the principal axes of bending. The remaining terms coupling the shear and torsion behavior, K_{23}, K_{24}, and K_{34}, indicate that the selected coordinate system is not at the shear center of the cross-section and thus can be used to determine the shear center and the principal axis of shearing. The discrepancies between the predicted and measured values indicate that the shear center and centroid do not exactly coincide between the model and actual blade, with the differences likely due to small dissimilarities in the geometry.

To study the impact of the material properties on the stiffness matrix, both the mean properties reported by the vendor and the properties with the Young's moduli and shear modulus reduced by 10% were considered, with the results shown in Table 7. The measured values for the axial and bending stiffness entries, K_{11}, K_{15}, K_{16}, K_{55}, K_{56}, and K_{66}, all remain nearly constant when changing the material properties used in the numerical model. When comparing with the numerical predictions for these terms, it can be observed that the reducing the vendor provided material properties by 10% provided much better agreement, with underpredictions of 1.3% and 0.5% on the axial and flap bending stiffness, and an overprediction of 3.9% on the lag bending stiffness. Similar to the composite beam, the measured values for the lag and tor-

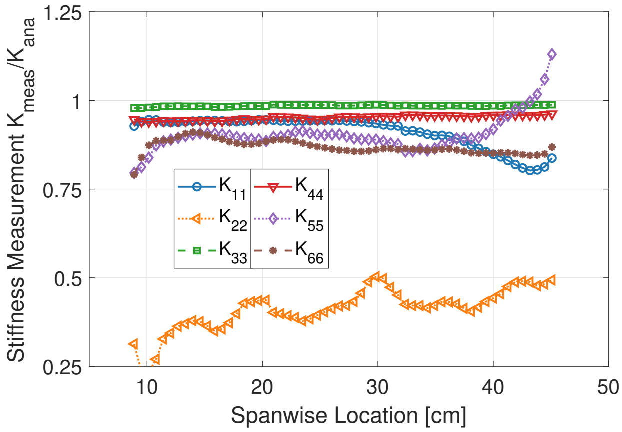

Fig. 21: Variation of the diagonal stiffness matrix entries along the span for the composite blade.

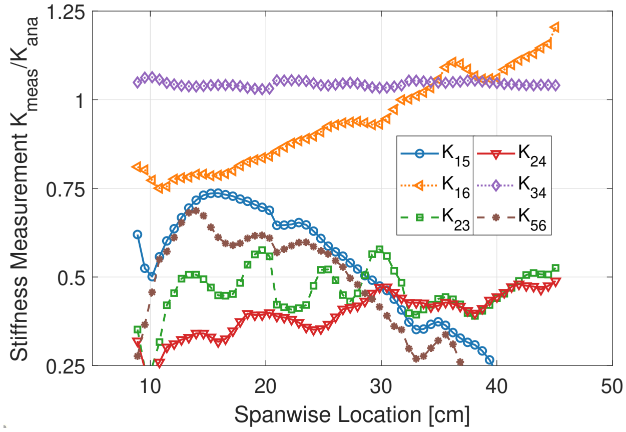

Fig. 22: Variation of the off-diagonal stiffness matrix entries along the span for the composite blade.

sion stiffness entries, K_{22}, K_{23}, K_{24}, K_{33}, K_{34}, and K_{44}, are all impacted by the change in material properties, which indicates that the warping field, predicted by the numerical model, only plays a significant role in predicting the shear and torsion stiffness values.

Table 7: Comparison of average composite blade stiffness values.

Stiffness entry	Mean material properties		10% reduced properties	
	Numerical	Measured	Numerical	Measured
K_{11}, N	5.92×10^5	5.40×10^5	5.33×10^5	5.40×10^5
K_{15}, N-m	8.67×10^2	4.12×10^2	7.80×10^2	4.12×10^2
K_{16}, N-m	-3.77×10^3	-3.54×10^3	-3.39×10^3	-3.54×10^3
K_{22}, N	7.58×10^5	3.11×10^5	6.82×10^5	3.10×10^5
K_{23}, N	1.70×10^4	7.80×10^3	1.53×10^4	7.25×10^3
K_{24}, N-m	-1.76×10^3	-6.93×10^2	-1.58×10^3	-7.09×10^2
K_{33}, N	1.74×10^4	1.72×10^4	1.57×10^4	1.55×10^4
K_{34}, N-m	4.36×10^2	4.56×10^2	3.93×10^2	4.13×10^2
K_{44}, N-m^2	4.76×10^1	4.53×10^1	4.28×10^1	4.13×10^1
K_{55}, N-m^2	7.89	7.13	7.10	7.13
K_{56}, N-m^2	-1.26×10^1	-4.87	-1.13×10^1	-4.87
K_{66}, N-m^2	3.48×10^2	3.02×10^2	3.14×10^2	3.02×10^2

5.4. Comparison to Other Methods

Among the methods currently used to measure the stiffness properties of beams, the most common approaches rely on measurements of either the displacements of the beam or the rotations of the beam to calculate the stiffness values. For a displacement based method, the beam is subjected to a known force, typically done with either a clamped-free setup or a three-point bending setup, and the displacement is measured, either through a contact method, such as a dial indicator, or a non-contact method, such as DIC. The current measurements are preformed using a clamped-free setup, which means that the flap bending and lag bending stiffness along the span can be calculated according to

$$K_{55} = \frac{F_z x^2(3l - x)}{6z} \tag{12a}$$

$$K_{66} = \frac{F_y x^2(3l - x)}{6y} \tag{12b}$$

where F_y and F_z are the applied tip forces, x is the distance from the clamped boundary, l is the length of the beam, z is the flapwise deflection, and y is the lagwise deflection. For a rotation based method, the beam is subjected to a known force and the rotation is measured. Direct measurements of the rotation can be performed using inclinometers or through the mirror method, which uses laser light deflected off mirrors attached to the surface to measure the rotation angle. While DIC does not directly measure the beam rotation, the displacement data is measured along a significant portion of the span and numerical differentiation can be used to estimate the rotation. For a clamped-free setup, the torsion, flap bending, and lag bending stiffness values can be calculated along the span according to

$$K_{44} = \frac{M_x x}{\theta_x} \tag{13a}$$

$$K_{55} = -\frac{F_z x(2l - x)}{2\theta_y} \tag{13b}$$

$$K_{66} = \frac{F_y x(3l - x)}{2\theta_z} \tag{13c}$$

where M_x is the applied torsional moment, θ_x is the torsional rotation, θ_y is the flap rotation, and θ_z is the lag rotation.

Figure 23 shows the comparison of the displacement based, slope based, and current methods for both the flap bending and lag bending stiffness values of the aluminum beam, normalized by the predicted value. For flap bending, the average stiffness calculated from the displacement method was 54.8 N-m^2, which was 86.9% of the predicted value of 63.1 N-m^2. When using the slope method, the average calculated stiffness increased to 58.1 N-m^2, which was still only 92.1% of the predicted value. For lag bending, the average stiffness from the displacement method was 3872 N-m^2, which was only 14% of the expected value of 27800 N-m^2. Using the slope method, the average stiffness nearly doubled to 7757 N-m^2, which was 27% of the predicted value. For tor-

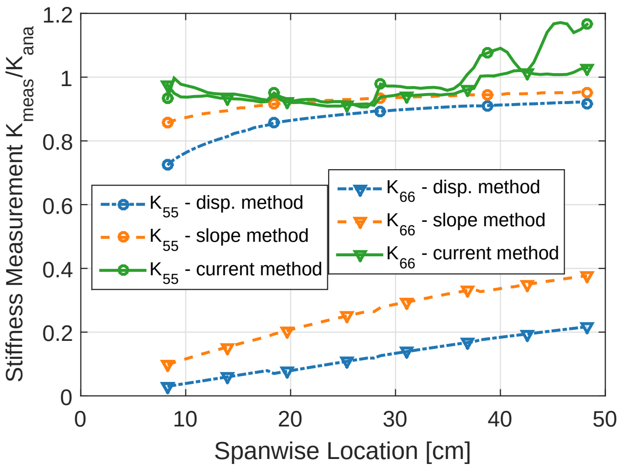

Fig. 23: Comparison of the current approach to other common measurement techniques.

sion, the stiffness calculated from the cross-sectional rotation was 79.4 N-m^2, which was 86.2% of the predicted value of 92.1 N-m^2. While these discrepancies were likely a result of the test stand not providing a perfect clamped boundary condition, the stiffness values calculated using the current approach were not strongly impacted by the boundary condition and provided much better agreement with the expected results.

6. CONCLUSIONS

A novel experimental-numerical technique for evaluating the full 6 × 6 stiffness matrices for beams has been presented, including results for three different beams. The general formulation allowed all the stiffness matrix coefficients to be calculated, without needing to reformulate the equations based on knowledge of expected coupling behavior. Digital Image Correlation (DIC) was used to experimentally measure the strain distribution on the surface of the blade, while the numerical analysis was performed using a 2-D finite element code, *SectionBuilder*, which was required for calculating the warping field. The input material properties were varied for both the composite beam and blade, to determine the sensitivity of the method to the numerical model. The following key conclusions were drawn from this study:

1. The coefficients along the diagonal of the stiffness matrix showed generally good agreement between the measured and predicted values. The lag shearing stiffness, K_{22}, showed the greatest variations, both along the span and with respect to the predicted values, due to the fact that smaller strains were expected and the beams were less stable when subjected to lateral forces. However, both the lag and flap shear stiffness, K_{22} and K_{33}, are usually neglected in most analyses (set to infinity), with differences of even an order of magnitude having an insignificant effect on the dynamic response of blades.

2. The method is also capable of capturing important coupling behavior in beams. From the composite beam, the measured flap bending/torsion coupling shows good agreement with the numerically predicted value; however, the less significant axial/shear coupling was not captured. In the composite blade, all six terms terms governing the location of the centroid and shear center as well as the principal axes of bending and shearing were measured experimentally. While discrepancies were observed between the measured and numerical values for most of these terms, these are due to small differences between the model and actual manufactured blade, in terms of both material properties and geometry.

3. The shear and torsion stiffness entries showed variations with changes in material properties, indicating the need for an accurate numerical model, particularly for the warping field, in addition to the experimental measurements when calculating these terms. However, the calculated axial and bending stiffness values remained nearly constant, indicating that these values were determined entirely by the experimental results. While only the average vendor reported material properties and the properties reduced by 10% were considered in the current study, the fact that the axial and bending stiffness values were entirely determined from the experiments can be used to refine the input material parameters, such that the predicted and measured stiffness values have the best agreement. This can in turn be used to provide more accurate numerical models for prediction of the stresses and strains during rotorcraft operations.

4. When compared with other common approaches for calculating the stiffness values, the current method was found to provide much better agreement with the predicted values. While the discrepancies in the other methods likely arose from not having a perfect clamp condition at the root of the beams, the current method relies only on measurements of the force and strains and is therefore not strongly affected by the boundary condition.

Overall, producing larger strains was important in improving the signal to noise ratios of the DIC measurements, but limitations on the maximum applicable loads, maximum allowable deflections, and localized buckling provided constraints on the maximum achievable strains. Additional investigations into an in-depth error analysis are currently ongoing, to provide bounds on the measured properties and identify the key features required for an accurate measurement.

ACKNOWLEDGEMENTS

This work was performed at the University of Maryland Alfred Gessow Rotorcraft Center under Army Aeroflightdynamics Directorate funding through the Vertical Lift Research Center of Excellence (VLRCOE), with technical monitoring from Dr. Mahendra Bhagwat. Tyler Sinotte is supported by the Clark Doctoral Fellowship Program.

COPYRIGHT STATEMENT

REFERENCES

[1] Kufeld, R., Balough, D., Cross, J., Studebaker, K., Jennison, C., and Bousman, W., "Flight Testing of the UH-60A Aircraft," American Helicopter Society 50th Annual Forum Proceedings, May 11-13 1994.

[2] Jung, S. and Lau, B., "Determination of HART I Blade Structural Properties by Laboratory Testing," NASA-CR-2012-216039, NASA Ames Research Center, Aug. 2012.

[3] Jung, S., You, Y., Dhadwal, M., Hagerty, B., Riemenschneider, J., and Keimer, R., "Blade Property Measurement and its Assessment on Air/Structural Loads of HART II Rotor," American Helicopter Society 70th Annual Forum Proceedings, May 20-22 2014.

[4] Fedorov, V. and Berggreen, C., "Bend-twist Coupling Potential of Wind Turbine Blades," *Journal of Physics: Conference Series*, Vol. 524, (1), 2014.

[5] Fleming, G. and Gorton, S., "Measurement of Rotorcraft Blade Deformation Using Projection Moiré Interferometry," *Shock and Vibration*, Vol. 7, (3), Mar. 2000, pp. 149–165.

[6] Sekula, M., "The Development and Hover Test Application of a Projection Moiré Interferometry Blade Displacement Measurement System," American Helicopter Society 68th Annual Forum Proceedings, Fort Worth, TX, 2012.

[7] Uehara, D., Eitner, M., and Sirohi, J., "Automated Operational Modal Identification of a Rotor Blade," American Helicopter Society 74th Annual Forum Proceedings, Phoenix, AZ, May 14-17, 2018.

[8] Giavotto, V., Borri, M., Mantegazza, P., Ghiringhelli, G., Carmaschi, V., Maffioli, G., and Mussi, F., "Anisotropic Beam Theory and Applications," *Computers & Structures*, Vol. 16, 1983, pp. 403–413.

[9] Bauchau, O. and Han, S., "Three-Dimensional Beam Theory for Flexible Multibody Dynamics," *Journal of Computational and Nonlinear Dynamics*, Vol. 9, (4), 2014.

[10] Han, S. and Bauchau, O., "Nonlinear Three-Dimensional Beam Theory for Flexible Multibody Dynamics," *Multibody System Dynamics*, Vol. 34, (3), July 2015, pp. 211–242.

[11] "Newport 321 Product Data Sheet," `https://www.rockwestcomposites.com/media/wysiwyg/Product_Categories/Materials_Tools/Newport_321_-_Resin_System.pdf`, 2006.

[12] "HexPly 8552 Product Data Sheet," `https://www.hexcel.com/user_area/content_media/raw/HexPly_8552_us_DataSheet.pdf`, 2016.

[13] Ho, J., "Stiffness Constants of Homogeneous, Anisotropic, Prismatic Beams," *AIAA Journal*, Vol. 53, (2), Feb. 2015, pp. 473–478.

[14] Ho, J., "Shear Stiffness of Homogeneous, Orthotropic, Prismatic Beams," *AIAA Journal*, Vol. 55, (12), December 2017, pp. 4357–4363.

[15] Wichita State University, *Composite Materials Handbook, Volume 2: Materials Properties*, SAE International, Warrendale, Pennsylvania, 2012.